ADVANCED MATERIALS
www.advmat.de

4D Additive–Subtractive Manufacturing of Shape Memory Ceramics

*Guo Liu, Xiaofeng Zhang, Xinya Lu, Yan Zhao, Zhifeng Zhou, Jingjun Xu, Jianan Yin, Tao Tang, Peiyu Wang, Shenghui Yi, Jiafeng Fan, Xueshi Zhuo, Yu Hin Chan, Wui Leung Wong, Haidong Bian, Jun Zuo, Yu Dai, Jian Wu, and Jian Lu**

The development of high-temperature structural materials, such as ceramics, is limited by their extremely high melting points and the difficulty in building complicated architectures. Four-dimensional (4D) printing helps enhance the geometrical flexibility of ceramics. However, ceramic 4D printing systems are limited by the separate processes for shape and material transformations, low accuracy of morphing systems, low resolution of ceramic structures, and their time-intensive nature. Here, a paradigm for a one-step shape/material transformation, high-2D/3D/4D-precision, high-efficiency, and scalable 4D additive–subtractive manufacturing of shape memory ceramics is developed. Original/reverse and global/local multimode shape memory capabilities are achieved using macroscale SiOC-based ceramic materials. The uniformly deposited Al_2O_3-rich layer on the printed SiOC-based ceramic lattice structures results in an unusually high flame ablation performance of the complex-shaped ceramics. The proposed framework is expected to broaden the applications of high-temperature structural materials in the aerospace, electronics, biomedical, and art fields.

1. Introduction

Additive manufacturing (AM) of structural materials is an active area in multidisciplinary research.[1] Existing three-dimensional (3D) printing systems exhibit high printing speed and scalability.[2] However, a tradeoff exists between the printing resolution and printing scalability or speed for many materials.[1] This tradeoff can be eliminated by integrating AM and subtractive manufacturing (SM) processes, and the concept of additive–subtractive manufacturing (ASM) can facilitate the development of rapid, precise, and scalable 3D printing technologies.[3]

The development of 3D printing systems has been limited by the extremely high melting points of high-temperature materials.[1,4] Meanwhile, the introduction of origami/kirigami-inspired strategy[5] has led to advancements in four-dimensional (4D) printing techniques.[6] By developing 4D printing materials with morphing capabilities and implementing control with different external stimuli (such as magnetic fields,[7] electric fields,[8] pneumatic deformations,[9] chemical reactions,[10] or their combinations), bottlenecks in the application of structural materials in various sophisticated and demanding operational environments can be addressed. The evolution of printable polymeric precursor materials and morphing systems has facilitated the emergence of 3D/4D printing technologies for

G. Liu, T. Tang, S. Yi, J. Lu
Centre for Advanced Structural Materials
City University of Hong Kong Shenzhen Research Institute
Greater Bay Joint Division
Shenyang National Laboratory for Materials Science
Shenzhen 518057, China
E-mail: jianlu@cityu.edu.hk

G. Liu, J. Lu
CityU-Shenzhen Futian Research Institute
Shenzhen 518045, China

The ORCID identification number(s) for the author(s) of this article can be found under https://doi.org/10.1002/adma.202302108

DOI: 10.1002/adma.202302108

G. Liu, X. Lu, Z. Zhou, Y. H. Chan, W. L. Wong, J. Lu
Hong Kong Branch of National Precious Metals Material Engineering Research Center
City University of Hong Kong
Hong Kong 999077, China

G. Liu, X. Zhang, Y. Zhao, J. Yin, P. Wang, H. Bian, J. Lu
Department of Mechanical Engineering
City University of Hong Kong
Hong Kong 999077, China

X. Zhang, J. Fan, X. Zhuo
National Engineering Laboratory for Modern Materials Surface Engineering Technology & The Key Lab of Guangdong for Modern Surface Engineering Technology
Institute of New Materials
Guangdong Academy of Science
Guangzhou 510650, China

X. Lu, J. Lu
Department of Materials Science and Engineering
City University of Hong Kong
Hong Kong 999077, China

high-temperature materials such as ceramics,[2a,11] glass,[2b,12] and metals.[11c] The aforementioned printing technologies can be divided into four types: 4D printing with two-step shape and material transformations upon contact stimuli,[11a] 4D shaping with cast molding,[11b] origami/kirigami with manual folding,[11c–e,12a] and 3D printing.[2a,b,11f,g,12b]

The integration of polymer-derived ceramics (PDCs) and AM techniques enhances the geometrical flexibility and mechanical properties of the resulting materials.[11g,13] Furthermore, the size of the printed PDC structures is increasing[2a] and the manufacturing process is becoming faster.[11f] Our team developed the first ceramic 4D printing system in 2018, which allowed the printing, deformation, and transformation of elastomer-based ceramic precursors into ceramic structures.[11a] This work was listed by the European Commission as one of the 4D printing cases in the "100 Radical Innovation Breakthroughs for the Future".[14] However, the practical application of existing ceramic 4D printing systems is limited owing to the time-intensive nature of the two-step shape and material transformations, low precision, and the requirement of mechanical contact stimuli for morphing. Moreover, the configuration of existing 4D printed ceramics cannot be changed. Unlike 4D printed shape memory alloys (SMAs),[15] the development of shape memory ceramics (SMCs) is severely limited by key factors, including material universality, geometrical flexibility, structural dimensions, and flexibility of shape memory capability.[16] Hence, a novel paradigm involving a one-step shape/material transformation of SMCs from noncontact stimuli and synergies between manufacturing speed, resolution, and scalability need to be established to promote the further development of ceramic 4D printing.

2. Results and Discussion

2.1. 4D Printing and the Ancient Ceramic Arts

The proposed 4D ASM of ceramics was inspired by traditional ceramic arts (**Figure 1**). From the Neolithic to the Northern Song Dynasty of ancient China, the manual machining in the green body of ceramics was versatile, including "Louhua" (cutting), "Kehua" (engraving), and "Tihua" (negative/positive engraving). In the Jin Dynasty of ancient China, an interesting art called "Tiaodao" was developed by ceramic artists to form delicate ornamentation on the surface of ceramics, which is a semi-automatic engraving of the green body with the assistance of a rotating turntable and a manually operated blade. With the development of laser technology, precursor laser cutting and engraving methods have emerged in two ceramic processing techniques: computer-aided manufacturing of laminated engineering materials (CAE-LEM) and low-temperature co-fired ceramics (LTCC).[17] However, the precursor materials utilized in the aforementioned arts and techniques are not stretchable, hindering the development of the 4D ASM of ceramics.

In this study, we developed silicone-based composite precursors to achieve improved geometrical flexibility, and we applied blade coating (2D AM) or direct ink writing (DIW, 3D AM) to generate elastomeric ceramic precursors. Meanwhile, SM techniques with a high-energy beam (e.g., a laser beam) can enhance manufacturing precision, resulting in a high-resolution ASM system. The 2D/3D AM-ed elastomeric precursors were laser-engraved or cut using the optimal laser scanning strategy in terms of laser scanning power and speed and subjected to heat treatment to obtain structural ceramics. Furthermore, 4D printing of ceramic materials has been developed by tuning heterogeneous precursors. By integrating the elastic precursor laser cutting/engraving (EPLC/EPLE) technique and the ceramic 4D printing technique, a complex-shaped, high-resolution, cost-efficient, and environmentally friendly 4D ASM paradigm for ceramic materials was developed in this work. This fully embodies the integration of modern advanced manufacturing technologies with ancient ceramic arts.

2.2. 4D Printed Shape Memory Ceramics

A representative ceramic 4D printing strategy is illustrated in this work (**Figure 2**). As shown in Figure 2A, the laser machining technique was used to generate high-resolution features and to tune the stiffness of the structures. Subsequently, a thin film was created on the surface of the sample, and the film thickness was tuned by changing the processing time in an ultraviolet (UV)/ozone system. The samples were subjected to heat treatment in inert gas or vacuum conditions. The thermal expansion and shrinkage behaviors of the 2D UV/ozone film material and 3D printed precursor material were different, and this heterogeneity led to the shape transformation of the precursor structures. In addition, owing to the different thermal shrinkage behaviors of the materials derived from the film and precursor materials, 4D printed first-generation EDCs can be further deformed by global or local heat treatment in the air, resulting in second-generation or first/second-generation composite EDCs.

A rapid one-step shape/material transformation of the heterogeneous structural precursors was achieved in an induction heating furnace (Figure 2B; Figure S1 and Movie S1, Supporting Information). The material and shape transformations of the engineered heterogeneous ceramic precursors could be simultaneously achieved in a few seconds with a heating rate of 1000 °C min^{-1} (Figure S2, Movies S2 and S3, Supporting Information), which is 100× as fast as in the conventional resistance heating approach for material transformation in existing

Y. Zhao
State Key Laboratory of Advanced Design and Manufacturing for Vehicle Body
College of Mechanical and Vehicle Engineering
Hunan University
Changsha 410082, China
J. Xu, J. Zuo
Shenyang National Laboratory for Materials Science
Institute of Metal Research
Chinese Academy of Sciences
Shenyang 110016, China
Y. Dai, J. Wu
School of Physics and Materials
Nanchang University
Nanchang 330031, China

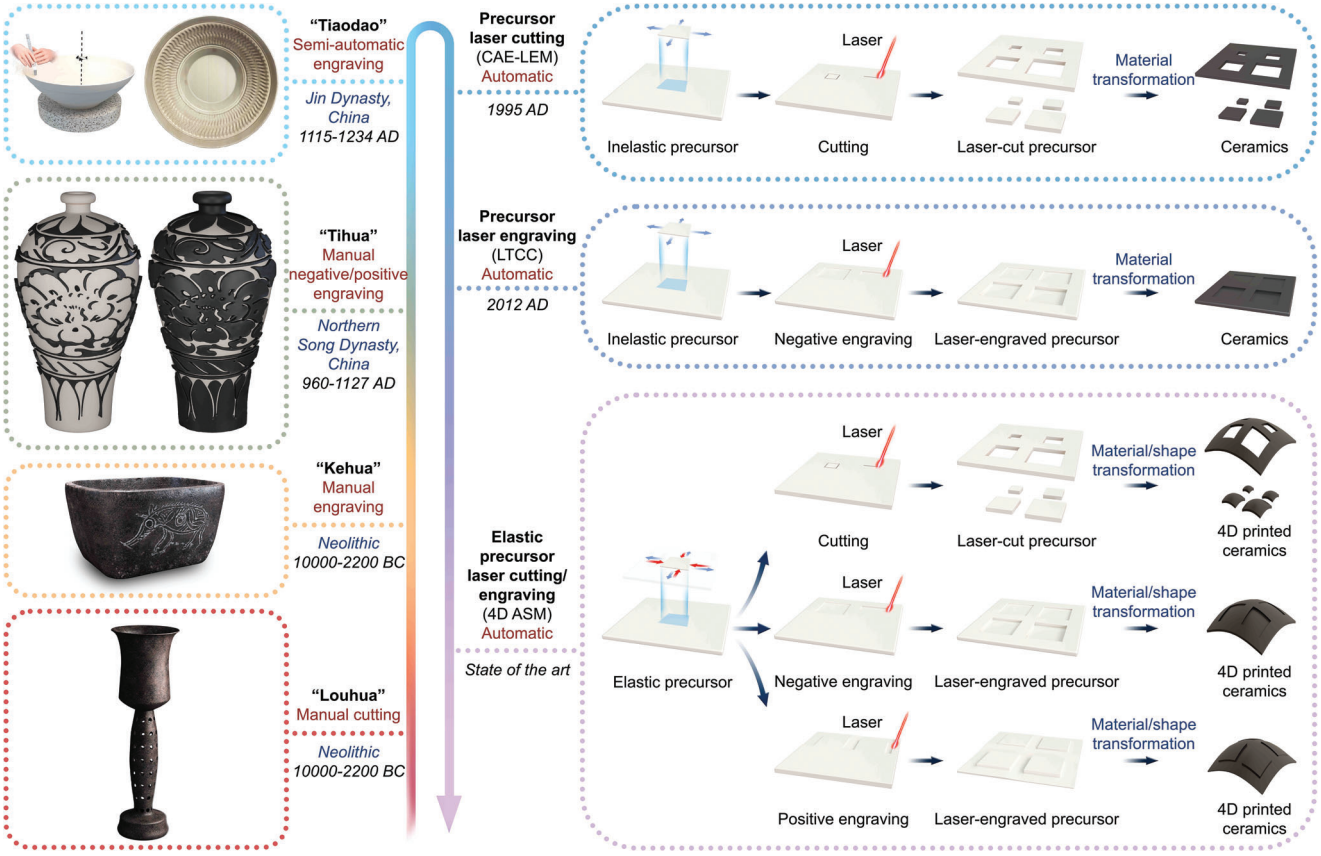

Figure 1. Schematic of 4D ASM of ceramics and EPLE/EPLC method inspired by traditional ceramic arts.

ceramic 4D printing systems.[11a] Induction heating is a highly efficient, energy-saving, and environmentally friendly heating method with a wide range of applications such as metal melting, surface heat treatment, and ceramic composite sintering. Induction heating converts electrical energy into thermal energy and has a high utilization rate of electrical energy, with a heating efficiency of over 90% and an energy consumption of only 1/3 of that of conventional heating. A smooth boron nitride (BN) plate was selected as the substrate because BN is well known for its excellent thermal stability and low-friction behavior. The BN substrate was also used to reduce the friction and sticking that could lead to forces being imparted on the object during shape deformation. Videos of the shape and material transformations of the ceramic precursors, located in three different ways (UV/ozone film facing up, down, or side) on the BN substrate, were recorded and compared to study the influence of the object interactions with the substrate on the shape transformation of the ceramic precursors. The object located with the UV/ozone film facing down easily fell during heating, and the three resulting first-generation EDCs exhibited similar shapes (Figure S2, Supporting Information). Hence, the location with the UV/ozone film facing upward was finally selected because the contact area between the object and the substrate for this type of location should be smaller than that for the UV/ozone film facing side.

In general, precise groove designs based on ASM (Figure S3, Supporting Information) can ensure versatility in building complex structures with zero, negative, positive, and mixed Gaussian curvatures.[18] Owing to the different thermal expansion and shrinkage behaviors of the heterogeneous structural precursors, the ceramic precursor was transformed in terms of both shape and material components when subjected to thermal treatment. Thermogravimetric analysis and differential scanning calorimetry showed that polymer-to-ceramic transformations were achieved at 300–900 °C (Figure S4A,B, Supporting Information). The Young's moduli of the PDMS/10 wt.% ZrO_2 and the UV/ozone microfilm were 1 and 13 MPa, respectively (Figures S4C and S5, Supporting Information). The elastomer and the UV/ozone film had an average composition of $SiO_{1.23}C_{1.45}Zr_{0.05}$ and $SiO_{3.13}C_{14.81}Zr_{0.01}$, respectively. The difference between the thermal expansion behaviors of the UV/ozone film and the elastomers (Figure S4D, Supporting Information) led to bending deformation (Figure 2B; Movie S1, Supporting Information). Moreover, the bending stiffness of the ceramic precursors and the curvatures of the resultant ceramics could be precisely tuned by modifying the depth and width of the laser-engraved grooves. Finite element analysis (FEA) simulations of the influence of thermal expansion on bending deformation were consistent with the experimental results (Figure 2C; Movie S4, Supporting Information). The precursors were transformed into ZrO_2–SiOC nanocrystalline-amorphous dual-phase (NCADP) ceramics with a porous feature (Figures S6–S8, Supporting Information) or amorphous SiOC glass (Figure S9, Supporting Information).

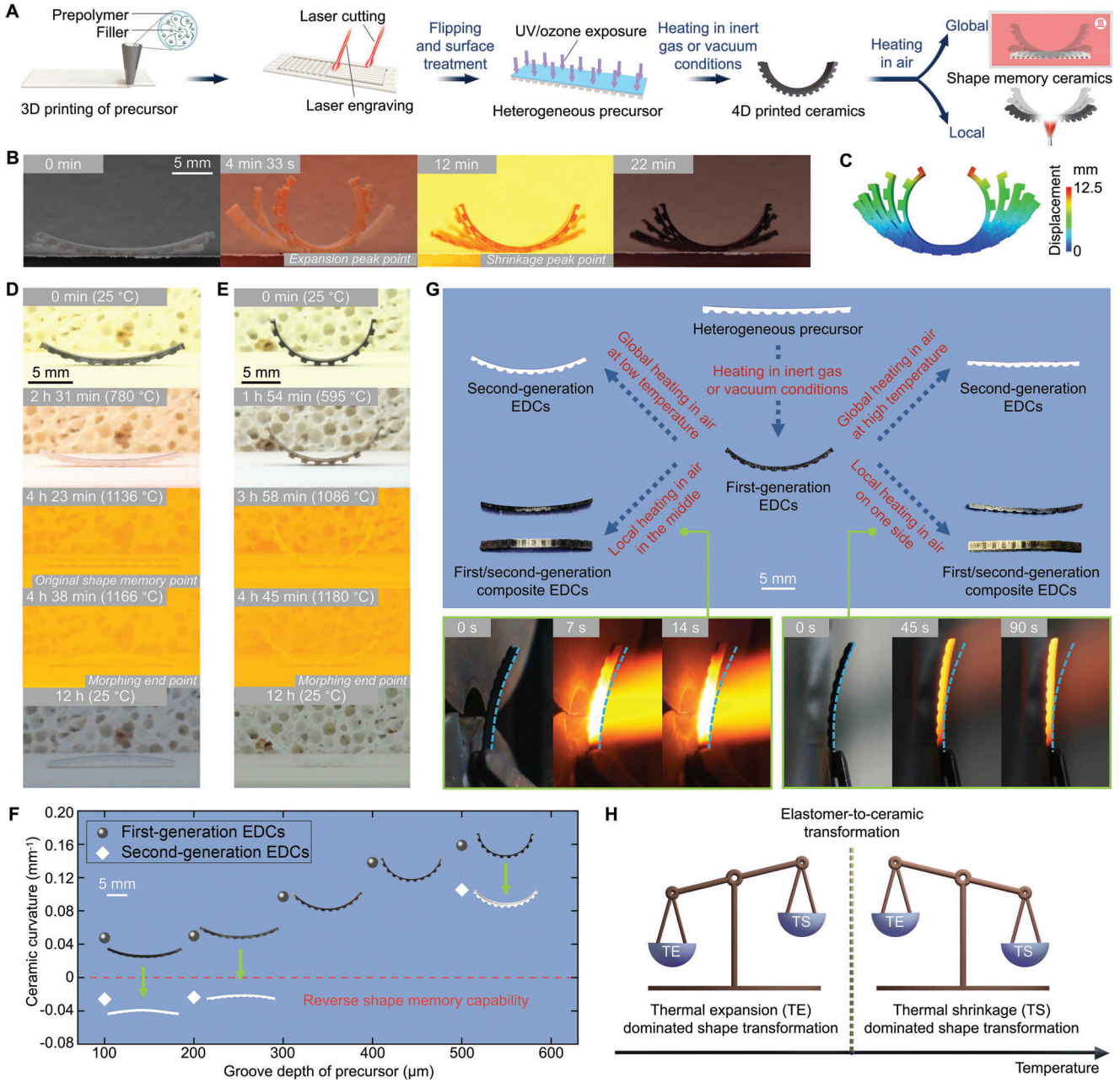

Figure 2. 4D ASM of SMCs. A) Schematic of engineering of heterogeneous precursors and 4D ASM of SMCs. B) Video of shape and material transformations of ceramic precursor structures (groove depth: 100–500 μm) generated using the strategy in Figure 2A, resulting in first-generation EDCs. C) The FEA simulation results are consistent with the experimental results for the thermal expansion process. D,E) Video of shape and material transformations of first-generation EDCs derived from ceramic precursors with groove depths of (D) 200 and (E) 500 μm, resulting in second-generation EDCs. F) Influence of the precursor groove depth on the curvature of the resulting first/second-generation EDCs with reverse shape memory capability. G) Global/local shape memory flexibility. H) The balance between thermal expansion and shrinkage effects serves as the mechanism for 4D printing.

4D printed ceramic structures demonstrated secondary self-morphing and reversible reconfigurability. When the sample was heated in air, the heterogeneity remained in the thermal shrinkage behavior of the first-generation elastomer-derived ceramics (EDCs) derived from the heterogeneous precursor. For the first-generation EDCs derived from the homogeneous precursor material of PDMS/10 wt.% ZrO_2 without UV/ozone treatment, the linear shrinkage ratios for heating in air at 1000 and 1200 °C were 3.5% and 5.6%, respectively. The configuration of the corresponding first-generation EDCs derived from the heterogeneous precursors subjected to UV/ozone treatment could be tuned for heating in the air under different conditions: the higher the heating temperature (below the morphing end point) applied on the first-generation EDCs, the more recovery to their original shape for the resultant second-generation EDCs. If the morphing end point was above the original shape

memory point, the first-generation EDCs would bend in the opposite direction and exhibit reverse shape memory capability. The ceramic materials were reversibly reconfigurable to the original planar shapes of the precursors and even to the reverse curved shapes of the first-generation EDCs under appropriate heating conditions, resulting in second-generation EDCs and original/reverse multimode shape memory behaviors of ceramics (Figure 2D–F; Figure S10 and Movies S5 and S6, Supporting Information). The ceramics had an average composition of $SiO_{1.65}C_{1.93}Zr_{0.07}$ and $SiO_{2.04}C_{0.83}Zr_{0.04}$ for the first- and second-generation EDCs, respectively. The crystal structures of the ceramics were analyzed through X-ray diffraction. The monoclinic ZrO_2 existed in the first-generation EDCs, while the tetragonal ZrO_2 and SiO_2 existed in the second-generation EDCs (Figure S11, Supporting Information). Similarly, local heat treatment in the air, such as heating in the middle or on one side, provided flexibility for the local receramization and self-morphing of first-generation EDCs, generating first/second-generation composite EDCs with multiple shapes (Figure 2G; Movie S7, Supporting Information).

In summary, before the elastomer-to-ceramic transformation, the difference in the thermal expansion coefficients of the precursor materials resulted in a first-stage shape transformation. After the elastomer-to-ceramic transformation, the differences in the thermal shrinkage ratios of the precursor materials resulted in a second-stage shape transformation with notable material transformation. When the resultant first-generation EDCs were heated in air, the heterogeneity in the thermal shrinkage behavior of the first-generation EDCs resulted in original/reverse multimode shape memory behaviors and receramization into the second-generation EDCs. The balance between thermal expansion and shrinkage is the mechanism for the 4D printing of ceramic materials (Figure 2H). Although engineering the expansion and shrinkage of materials is a common strategy for 4D printing,[19] this work represents a successful attempt at 4D printing of ceramics by recording the balance between thermal expansion and shrinkage.

The development of SMCs starts from the martensitic phase transformation. In this study, we proposed and demonstrated a completely new mechanism for SMCs, that is, heterogeneity in the thermal expansion–shrinkage behavior (**Table 1**). Based on the newly developed SMC fabrication mechanism (heterogeneity in thermal expansion–shrinkage behavior) in this study, versatile SiOC-based SMCs can be developed in a facile manner by the physical mixing of liquid silicone with varying ceramic fillers. Geometrical flexibility could be largely enhanced with 4D ASM (2D/3D printing + laser engraving/cutting of ceramic precursors) compared to the ceramic powder pressing used in previous studies. Furthermore, we extended the dimensions of structural SMCs from the microscale/mesoscale to the macroscale and achieved original/reverse and global/local multimode shape memory capabilities of ceramics. Thus, these aspects differentiate our work from existing studies on SMCs.

2.3. 4D Morphing Precision and Complexity

4D printing can achieve geometrical flexibility and high morphing precision for advanced structural ceramics and can be used in high-temperature applications, such as aerospace propulsion.[20] Two derivative demonstrations of the aforementioned ceramic 4D printing strategy are illustrated in this work (**Figure 3**,A,B). The ceramic engine turbine disk and 12 blades were 4D printed as a single piece and no assembly process was required (Figure 3C,D; Movie S8, Supporting Information). Through local UV/ozone exposure, blades with planar surfaces were simultaneously programmed to achieve twisting deformation with high repeatability, resulting in a flower-like symmetrical structure. The high repeatability demonstrates high manufacturing precision in 3D structuring and 4D shaping (Figure S12, Supporting Information). The FEA simulation of the influence of thermal expansion on twisting deformation was consistent with the experimental results (Figure 3E; Figures S13 and S14, and Movie S9, Supporting Information). Furthermore, shape memory behaviors were demonstrated with a complicated all-ceramic bladed disk (blisk) architecture, and twisted blades in first-generation EDCs could be tuned to the original planar shapes in second-generation EDCs at an original shape memory point of 1231 °C (Figure 3F; Figure S15 and Movie S10, Supporting Information).

The industrialization potential of this paradigm was demonstrated by the mass production capability of heterogeneous precursor materials assisted by a multistation turntable system. To enhance manufacturing speed, blade coating was implemented using an area-by-area printing strategy instead of DIW in the line-by-line printing strategy. The EPLC method and UV/ozone surface treatment ensured manufacturing precision for 3D structuring and 4D shaping, respectively. The proposed approach was used to prepare a 10 × 10 array of heterogeneous precursors for ceramic kirigami structures with delicate features and high repeatability within 50 min (30 s per product, average; Figure 3G; Figure S16 and Movie S11, Supporting Information).

Table 1. Differentiation of our study from previous representative works on SMCs.

Shape memory ceramics' composition for material universality	Processing method for geometrical flexibility	Structural dimensions	The flexibility of shape memory capability	Mechanism of shape memory ceramics
SiOC-based ceramics derived from elastic precursors [this study]	4D additive-subtractive manufacturing (2D/3D printing + laser engraving/cutting)	Macroscale (over 4 cm)	Original/reverse, global/local	Heterogeneity in thermal expansion–shrinkage behavior
$(Zr/Hf)O_2(YNb)O_4$ [H. Gu et al. Nature **2021**, 599, 416; Ref. 16d]	Ceramic powder pressing	Mesoscale (4 mm)	Original, global	Martensitic phase transformation
ZrO_2-based ceramics [A. Lai et al. Science **2013**, 341, 1505; Ref. 16b]	Ceramic powder pressing + focused ion beam	Microscale (6 μm)	Original, global	Martensitic phase transformation

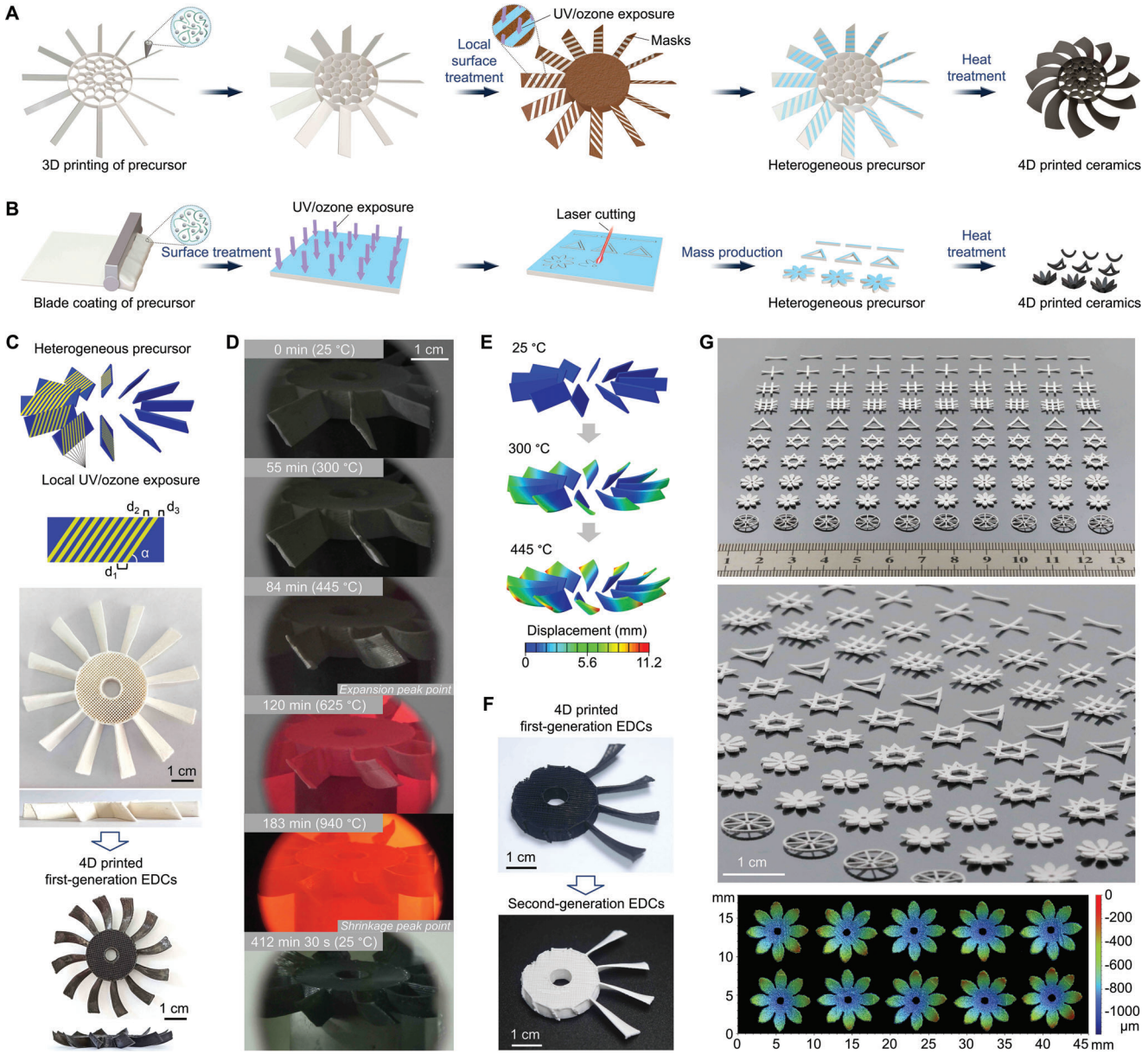

Figure 3. Geometrical complexity, manufacturing speed, and precision of ceramic 4D printing. A) 3D printing and local surface treatment offer the potential for enhancing geometrical complexity in 3D structuring and 4D shaping, respectively. B) Blade coating and laser machining (such as the EPLC method in the schematic) offer the potential for enhancing manufacturing speed and precision. C) 4D printed first-generation EDCs resulted from heterogeneous precursors generated using the strategy in Figure 3A. Definitions of important geometric parameters of local UV/ozone exposure: d_1 = 2 mm; d_2 = 1 mm; d_3 = 1.1 mm; α = 55°. D) Video of shape and material transformations of heterogeneous precursor, resulting in first-generation EDCs. E) FEA simulation results for the thermal expansion process in Figure 3D. F) Second-generation EDCs resulted from first-generation EDCs of 4D printed all-ceramic blisk. G) Mass production of a 10 × 10 array of ceramic kirigami structures generated using the strategy in Figure 3B and the repeatability in 10 demonstrations of 4D printed flower-type ceramic structures.

2.4. 3D Structural Resolution and Scalability

A mapping model for varying the laser scanning power and speed was established. Deeper features can be generated by increasing the laser scanning power and decreasing the laser scanning speed, and the depth of the features can be precisely adjusted in steps of ≈50 μm (**Figure 4**A). Upon the elastomer-to-ceramic transformation, the 3D architectures of the ceramic materials remained planar with uniform shrinkage, resulting in the retention of the global shape and local features.

The minimum feature size of the laser machining was 6 μm after ceramization (Figure S17A, Supporting Information), which was at least three times better than that associated with the DIW of ceramics (25 μm in previous studies).[21] The ASM system achieved synergy between resolution and scalability. Ceramic plates were subjected to PLE to demonstrate the

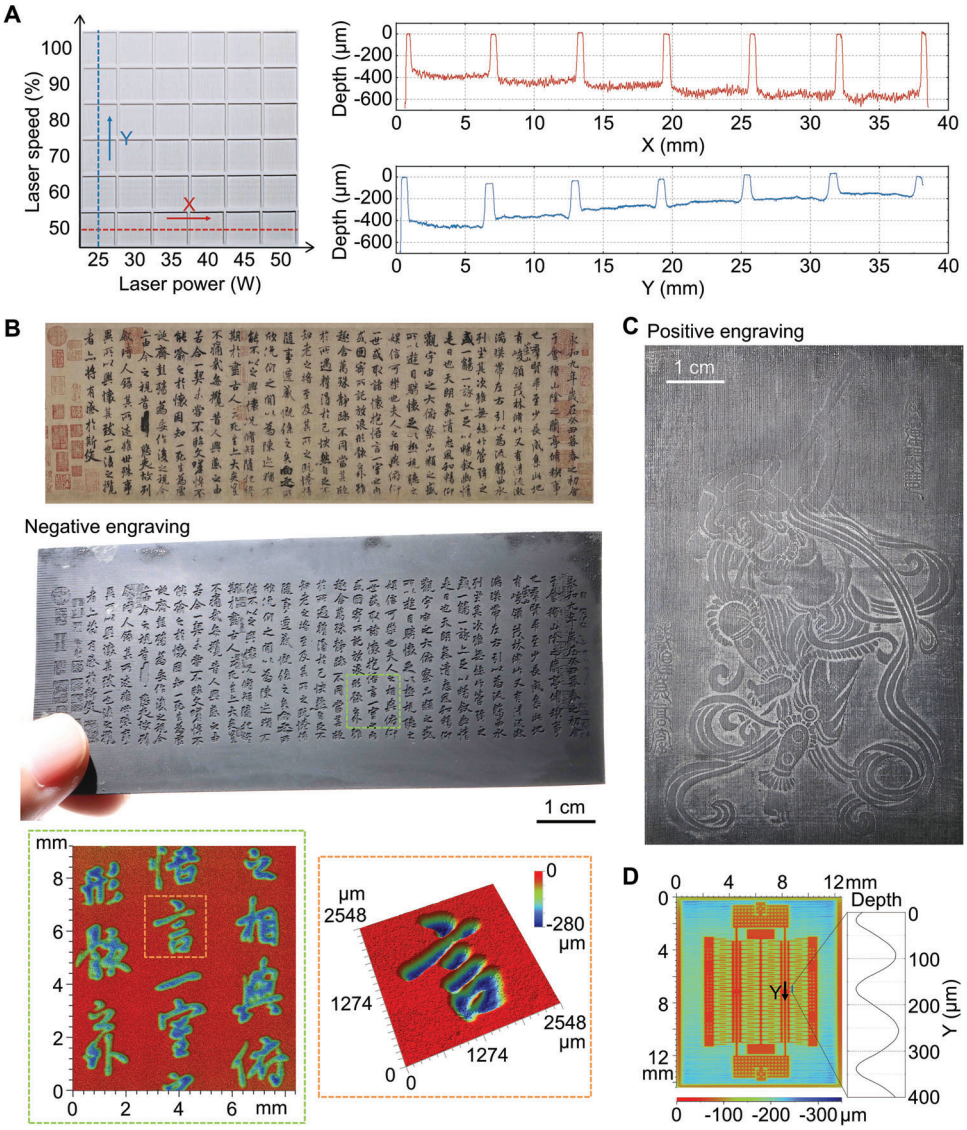

Figure 4. High-resolution EPLE method for ASM of ceramics. A) Precise adjustment of the engraved depth of the precursor material by the laser power and laser speed. The minimum depth feature size along the X and Y axes is 50 μm. B) Large-scale ceramic planar plates with a delicate negative engraving of Chinese traditional calligraphy characters in "Preface to the Poems Composed at the Orchid Pavilion" by Wang Xizhi in running script (copy version by Chu Suiliang; image source: the Palace Museum; http://www.dpm.org.cn/collection/handwriting/228277.html). https://en.dpm.org.cn/collections/collections/2011-03-31/1014.htmC) Large-scale ceramic planar plates with a delicate positive engraving of the mural character in Flying Apsaras in Dunhuang Murals. D) Laser-engraved ceramic precursor MEMS structure with a minimum feature size of 80 μm.

introduction of intricate 3D features into high-temperature materials, which is particularly useful for the research and restoration of cultural relics. Using the proposed method, we realized high-resolution negative engraving of 3D Chinese traditional calligraphy characters (Figure 4B; Figure S17B, Supporting Information) and delicate positive engravings of well-known artworks, such as the Flying Apsaras (Figure 4C; Figure S17C, Supporting Information).

Furthermore, a typical ceramic microelectromechanical system (MEMS) resonant strain sensor (length of over 10 mm; the depth and width of the tuning forks were ≈20 and 60 μm, respectively) was built (Figure 4D; Figure S17D–F, Supporting Information), and the design was based on a double-ended tuning fork (DETF) topology. In electronics such as MEMS devices, the resonant frequency shift of a DETF depends on the applied strain. At a given applied strain, printed large-scale or cascaded MEMS resonant-strain sensors are expected to exhibit large frequency shifts. The strain sensitivity can be enhanced by improving the scalability of strain sensors prepared using the EPLE method. In addition, ceramic MEMS resonant strain sensors are expected to be inherently resistant to elevated temperatures, temperature gradients, humidity, and other environmental factors. The temperature or humidity noise introduced in the highly sensitive measurement results can be minimized. Therefore, high-resolution, large-scale ceramic MEMS resonant strain sensors fabricated using ASM can exhibit enhanced sensitivity and

decreased environmental interference, particularly in harsh engineering environments.

2.5. 2D Surface Quality

The SM of precursors and 4D printing techniques can be applied in the post-processing of printed structures to address the stair–step effect resulting from layer-wise AM. High-energy beams or mechanical grinding tools can be used for surface polishing and eliminating the stair–step effect of 3D printed precursor materials. In this manner, smoother surfaces of similar or deformed ceramic structures than the surfaces of hybrid manufactured precursor materials can be obtained upon shrinkage during the material transformation to ceramic materials (**Figure 5**A). The surface roughness (Ra) of a printed 2D structure of the ceramic precursor was 16.5 μm, and it decreased by 44% (to 9.2 μm) after laser polishing (Figure 5B). In addition, the surface quality of a 3D printed hyper-hemispherical dome was enhanced by 84% (from Ra = 108.6 to 17.4 μm) owing to the mechanical grinding of its precursor and uniform linear shrinkage accompanying polymer-to-ceramic transformation (Figure 5C; Figure S18A, Supporting Information). The integration of precursor polishing and 4D morphing provides a new route for preparing high-surface-quality, high-temperature materials with complex shapes. For example, polishing the planar surface of blades in a blisk is easier than polishing curved surfaces. The surface roughness of the curved blade decreased by 65% and 37% after mechanical grinding and laser polishing, respectively (Figure 5D,E; Figure S18B–D, Supporting Information), which can help extend the lifespan of turbine blades.[22] The concept of 2D/3D/4D precursor polishing can be integrated with the AM process to form an ASM system (Figure S19, Supporting Information). Compared to a system involving a separate AM process for the precursor and precursor polishing, the integrated system can more efficiently and precisely manufacture structural ceramic materials with high surface quality, as the 3D architectural features can be directly and precisely shared by additive and subtractive manufacturing processes. The advantages of the hybrid system are more notable for products with higher geometrical complexities.

2.6. Thermal Performance

The ink system in the DIW technique can be easily tuned, leading to considerable flexibility in terms of material selection and performance optimization for high-temperature applications. Consequently, the material performance can be tailored in terms of the thermal and mechanical aspects. In this study, the 3D printed ceramic lattices possessed ZrO_2–SiOC or AlON–SiOC NCADP structures with nanopores (Figures S20 and S21, Supporting Information). SiOC is amorphous and softens at temperatures above 1200 °C, which could limit the high-temperature structural applications of the 4D ASM-ed SMCs. To improve the stability of SiOC, an a-Al_2O_3 layer was prepared on its surface by atomic layer deposition (ALD) in this investigation. The a-Al_2O_3 layer has a dense hexagonal structure that can effectively block the diffusion of external oxygen into the matrix and prevent the oxidation of SiOC, as described in Equation (1). Additionally, water-oxygen corrosion occurs in turbine engines. If SiOC is oxidized to form SiO_2, SiO_2 reacts with H_2O to form vapor $Si(OH)_2$ as described in Equation (2). However, based on the principle of thermal dynamics, a-Al_2O_3 has better corrosion resistance than SiOC. In addition, a-Al_2O_3 reacts with SiO_2 to form mullite ($3Al_2O_3{\cdot}2SiO_2$), as described in Equation 3. The mullite has a high melting temperature (1910 °C) and low thermal conductivity (≤0.35 W/(m °C)). Therefore, mullite can be used as a thermal barrier coating. Furthermore, the ALD technique can guarantee the evenness of thermal protection for 4D printed complex-shaped ceramics. Through the ALD of amorphous Al_2O_3 (Figure S22, Supporting Information), an Al_2O_3-rich layer was uniformly formed on the surface of the printed ligaments in the interior of the ceramic lattices, which is challenging to achieve using physical vapor deposition.[23] Thus, 4D printable structural ceramics from this study also exhibited an unusually high flame ablation performance.

$$SiOC + O_2 - SiO_2 + CO_2 \quad (1)$$

$$SiO_2 + H_2O - Si(OH)_2 \quad (2)$$

$$Al_2O_3 + SiO_2 - 3Al_2O_3 \cdot 2SiO_2 \quad (3)$$

The resulting Al_2O_3-deposited ZrO_2–SiOC (**Figure** 6A-C Figure S23, Supporting Information) and AlON–SiOC (Figure 6D-F Figure S24, Supporting Information) ceramic lattices exhibited significantly higher flame ablation performance than their counterparts not subjected to ALD, and the specific weight changes at 1400 °C (1 min application) were 97% lower than those of IN718 alloy lattices (Figure 6G,H; Figures S25–S27 and Table S1, Supporting Information). Moreover, Al_2O_3-deposited NCADP ceramic lattices exhibited a flame ablation performance (1400 °C, 1 min application) that was six times higher than that of the typical thermal barrier coating (TBC)-enhanced bulk IN718 alloy.[24] The average bulk density of the prepared ceramic lattices was 1.2–1.9 g cm^{-3}, 16–25% that of the TBC-enhanced bulk IN718 alloy (Figure 6H; Table S1, Supporting Information). The printed Al_2O_3-deposited ZrO_2–SiOC NCADP ceramics maintained their lattice structure with a limited specific weight change (0.9 mg cm^{-2}) at temperatures as high as 1500 °C (Figure 6I; Movie S12, Supporting Information). The comparison of Al_2O_3-deposited ceramic lattices with TBC-enhanced bulk IN718 alloy and IN718 alloy lattices offers the potential for the evolution of structural material systems in engines and the progression of corresponding temperature capabilities, thus leading to enhanced overall efficiency and decreased environmental pollution of aerospace propulsion components.[25] Furthermore, the mechanical properties of 4D printed ceramic architectures can be anticipated owing to their NCADP structures.[26]

2.7. Application Perspectives

The proposed method differs from other existing approaches in the manufacturing of structural ceramic/glass materials. Specifically, this study represents the first successful attempt at the 4D printing of SMCs, and also the first successful attempt at

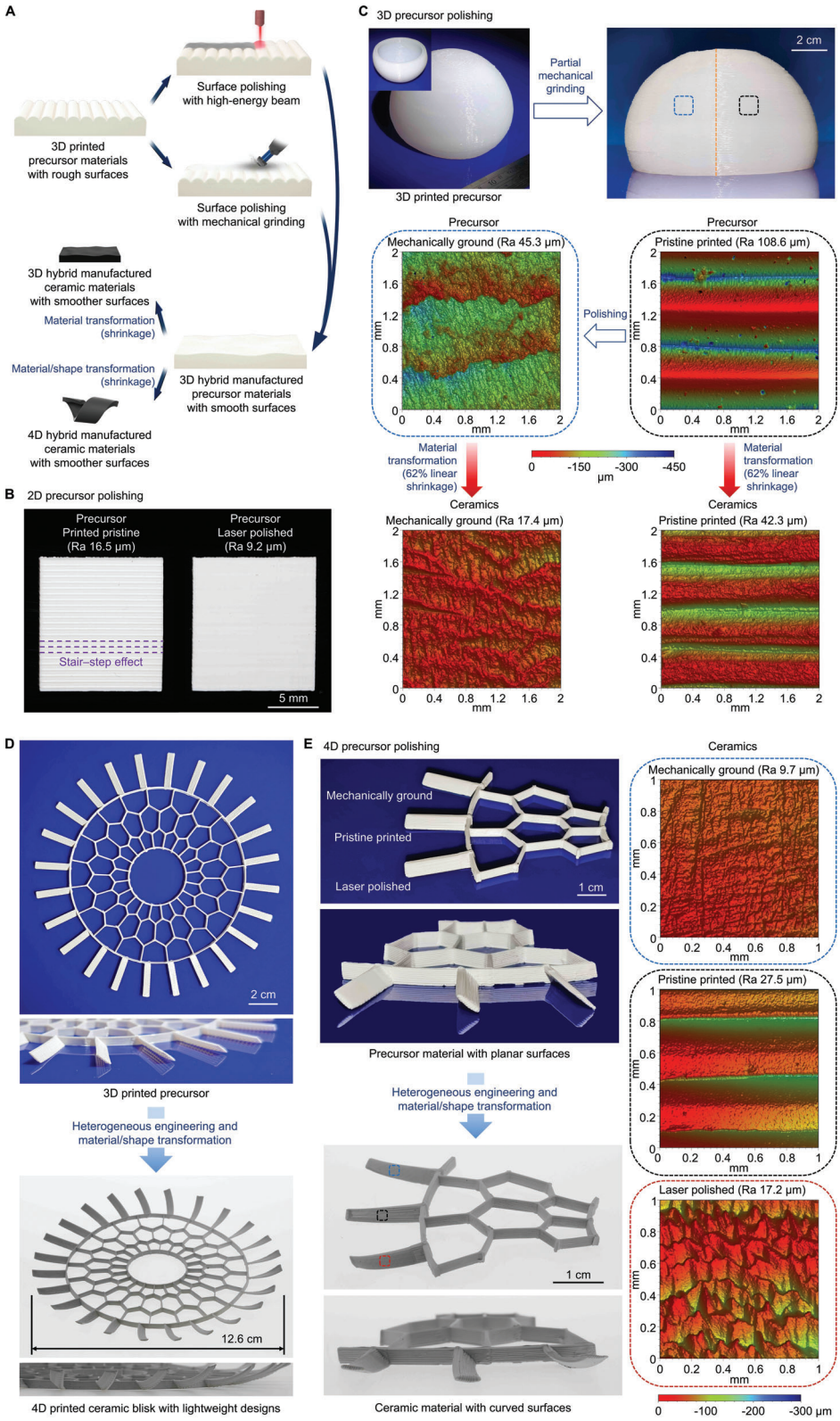

Figure 5. 2D/3D/4D precursor polishing. A) Precursor polishing strategy. B) EPLE method was used for polishing a printed planar ceramic precursor material with the stair–step effect. C) Mechanical grinding was performed for polishing a printed ceramic precursor material with a hyper-hemispherical dome structure, resulting in surface polishing of 3D printed ceramic structures through polymer-to-ceramic transformation. D) 4D printing and integrated shaping for a large-scale all-ceramic blisk with lightweight designs. E) 4D printing for polishing complex-shaped ceramic blades with curved surfaces.

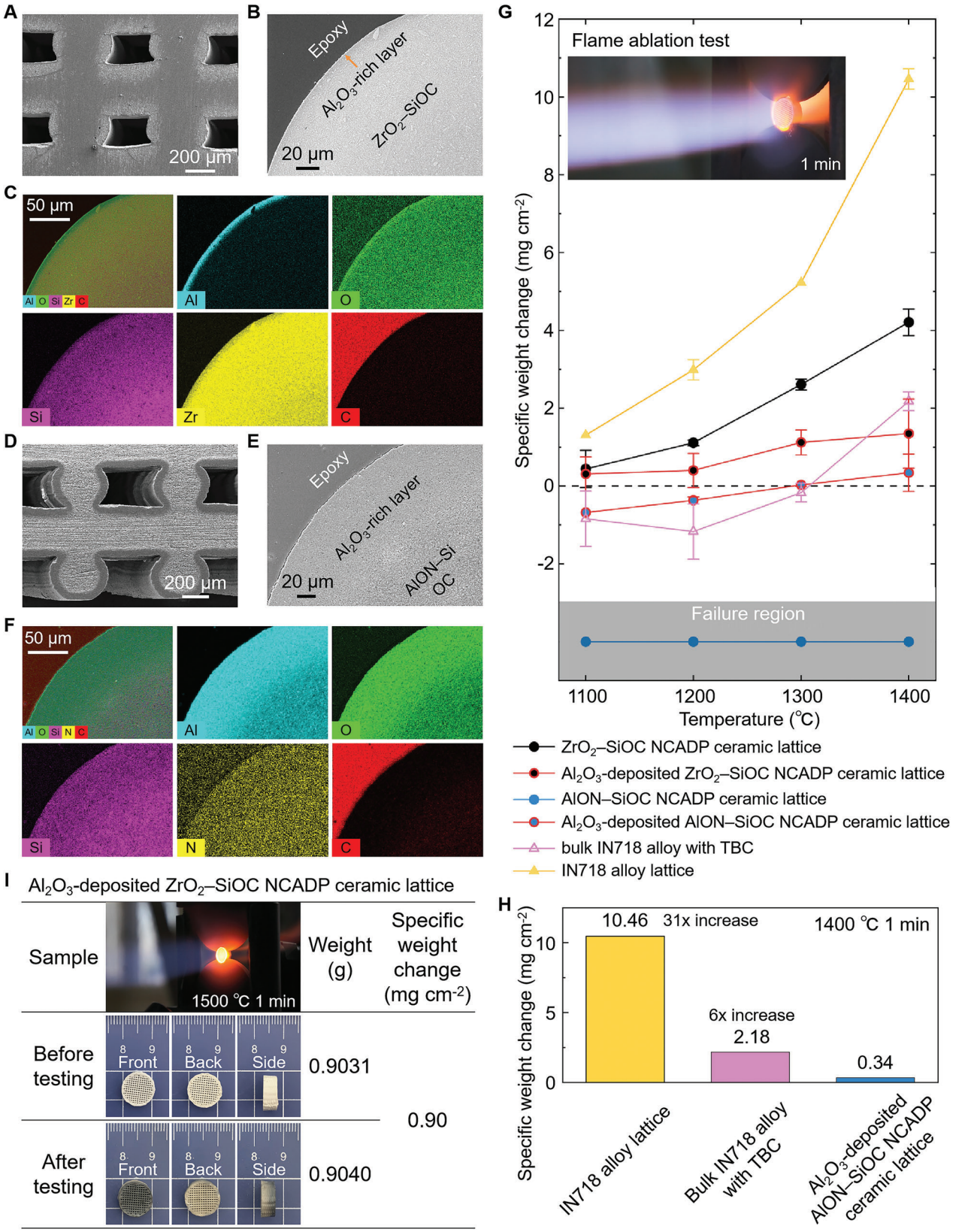

Figure 6. Thermal performance of printed ceramic materials. A–F) SEM images of the Al_2O_3-deposited ZrO_2–SiOC (A–C) and AlON–SiOC (D–F) ceramic lattices. G) Flame ablation tests. H) Comparison of flame ablation performance at 1400 °C for 1 min. I) Sample status of Al_2O_3-deposited ZrO_2–SiOC NCADP ceramic lattices before and after flame ablation testing at 1500 °C for 1 min.

the 4D printing of ceramic materials with ASM. Thus, the proposed approach differs from the reported methods for achieving geometrical flexibility. The proposed approach can overcome the scalability-resolution tradeoff among structural ceramic/glass manufacturing techniques (Figure S28, Supporting Information), and ensure high scalability (16 cm), high resolution (6 μm in minimum feature size), ultrafast transformation to high-temperature materials (in several seconds), and rapid manufacturing of precursor materials (mass production capability). The concept of 2D/3D/4D precursor polishing using versatile high-energy beams and mechanical grinding tools was developed to obtain high-surface-quality high-temperature materials. Furthermore, the proposed paradigm can be applied to various SiOC-based ceramic and glass materials. Thus, this study can broaden the application scope of high-temperature structural materials in aerospace, electronics, biomedical, and art domains, among other fields (**Figure 7**).

The concept of 4D printing and integrated shaping for all-ceramic aerospace turbine blisks is a valuable route for developing advanced and intelligent aerospace propulsion components with high system efficiency, low lifecycle costs, and decreased environmental pollution (Figure 7).[20b,25,27] First, the proposed 4D printing technique for ceramic materials overcomes the limitations encountered in fabricating geometrically complex large-scale (as large as 16 cm) propulsion components with topologically lightweight designs using conventional wrought, casting, welding, and SM techniques (Figure 5D).[28] The simple structure of the precursors can facilitate the precision machining of ceramic materials with complex shapes, such as in 4D precursor polishing (Figure 5E). Moreover, ceramic materials exhibit low density, high hardness, and excellent thermal stability (Figure 6H), and can operate at higher turbine inlet temperatures (higher than 1300 °C) with lower cooling air requirements and higher combustion efficiencies than those associated with conventional high-temperature alloys.[20b,25,27] Thus, the use of an all-ceramic blisk increases the engine thrust-to-weight ratio and overall efficiency in an eco-friendly manner while decreasing fuel consumption.[27] Furthermore, the integrated shaping of the blisk can decrease the assembly time and lifecycle costs and enable better control of the clearances between parts of the propulsion system (Figure 3C), thereby decreasing the vibration, wear, and noise resulting from assembly deviations.[27]

The concept of 4D printing can be applied in space exploration, such as in morphing thermal protection systems (Figure 7). Specifically, 4D printed SMCs (Figure 2D–G) can help enhance the flexibility of the thermal protection system of a re-entry vehicle/capsule. Using real-time measured data, an optimized and reliable thermal protection system with shape-morphing capabilities can be 4D printed in situ to address the shape-related uncertainties and variable thermal environments encountered by reentry vehicles/capsules owing to various factors such as ablation and complex flow effects. A lightweight design is preferable to the traditional design of heavy thermal shields to increase the payload and decrease the cost.

The proposed concept can be used in space for the on-orbit manufacturing of ultrahigh-performance turbine blades or on-orbit repair (such as additive remanufacturing) of heat shields and other essential parts that may fail in a long-term mission (Figure 7). Manufacturing and repair based on the proposed technique are more rapid and less expensive than traditional techniques because the placement of ultra-large-scale components in orbit or beyond is prohibitively expensive. The proposed 4D printing concept can also be applied to in situ space printing and colonization (Figure 7). In general, the ability to manufacture locally using local materials is key to colonizing any location in space.

Furthermore, hybrid 4D printing materials with integrated soft ceramic precursors and rigid ceramics, resulting from the local ceramization of precursor materials or multi-material printing/assembly, can facilitate the development of foldable ceramic cell phone backplates (Figure 7). Moreover, soft/rigid hybrid bioimplants that can adapt to complex and dynamic biological environments can be prepared (Figure 7).[29] The artistic nature of ceramics and their capability to form complex origami/kirigami structures and delicate features render them suitable for the research and restoration of cultural relics (Figure 4B,C) and the preparation of unique decorations and customized jewelry (Figure 7).[11a]

3. Conclusion

The proposed ASM system can be used to realize rapid, precise, and scalable manufacturing of ceramic materials by increasing the 3D printing efficiency from line-by-line printing to area-by-area printing.[1] The laser beam technique used in SM can be extended to other controlled high-energy flows such as electron beams, ion beams, high-pressure liquids, and a combination of these. The framework involving UV/ozone films on elastomeric polymers can be extended to other 2D AM materials such as metal films to achieve heterogeneous precursors.[30] Future work could aim to enhance the toughness of ceramic materials by engineering biomimetic soft/rigid hybrid polymer/ceramic material systems and structural/functional gradient ceramics by infiltrating 4D ASM-ed hierarchical ceramic architectures with polymer materials, local ceramization of precursor materials, local receramization of ceramic materials, or multi-material printing/assembly.[29,31]

Unlike SMAs, the development of SMCs is still at an early stage. This study will bring about significant improvements in this new area compared to SMAs, and the successful attempt at original/reverse and global/local multimode shape memory behaviors of ceramics opens the way to various types of self-morphing of SMCs. Although much work remains to be done to optimize the materials and processing for the further development and applications of SMCs, the unusual properties of the SMCs reported in this manuscript, as well as other ceramics that exhibit martensitic phase transformation, offer prospects for this area.

4. Experimental Section

Preparation of Materials: For the ceramic materials, the inks for the precursors shown in Figures 2, 3C,D, 4, and 5B consisted of ZrO_2 nanoparticles (Tong Li Tech Co. Ltd.) and poly(dimethylsiloxane) (PDMS, SE1700, Dow Corning). Either 10 or 20 wt.% ZrO_2 nanoparticles were added to the liquid PDMS and mixed using a triple roller mill (Exakt). The ink was then poured into a syringe and centrifuged. The ink used for the precursors shown in Figure 5C is silicone (DOWSIL™ Green Multiple Purpose Silicone Sealant). The ink for the precursors shown in Figure 5D,E consisted

Figure 7. Application perspectives of 4D ASM of SMCs.

of AlON nanoparticles (40–50 wt.%) and PDMS (SE1700, Dow Corning). The ink for the precursors shown in Figure 6A consisted of ZrO_2 nanoparticles (20–50 nm, Tong Li Tech Co. Ltd., 58 wt.%) and a mixture of two types of PDMS (SE 1700 and Sylgard 184, Dow Corning). The ink for the precursors shown in Figures 3G and 6D consisted of AlON nanoparticles (50 wt.%) and PDMS (SE1700, Dow Corning). For the SiOC glass, liquid PDMS ink (SE1700, Dow Corning) was poured into a syringe and centrifuged.

4D ASM: To realize the bending of heterogeneous ceramic precursors during the induction heating process, as shown in Figure 2B, solid precursors (22 mm × 2 mm × 0.8 mm) were 3D printed with PDMS/10 wt.% ZrO_2 ink using a DIW machine (Regenovo Biotechnology Co., Ltd.). The printed precursors were then cured in an oven at 150 °C for 30 min. The cured precursors were laser-engraved to generate 11 evenly distributed grooves on the top surfaces using CO_2 laser machining equipment (Epilog). The width of each groove was 1 mm, and their depths were 100, 200, 300, 400, and 500 µm. The samples were then flipped and subjected to UV/ozone treatment for 8 h. The prepared heterogeneous ceramic precursors were heated to 1300 °C within 12 min in an induction heating furnace with an argon flow of 200 mL min^{-1} and maintained this temperature for 10 min. To realize the shape memory behaviors, as shown in Figure 2D-F and Figure S10 (Supporting Information), the first-generation EDCs derived from ceramic precursors with groove depths of 100, 200, and 500 µm were then heated to 1300 °C for 30 min in air with a tube furnace, resulting in second-generation EDCs.

To realize the global shape memory behaviors, as shown in Figure 2G, the first-generation EDCs derived from PDMS/10 wt.% ZrO_2 were heated to 1000 or 1200 °C for 2 h in air with a tube furnace. To realize the local shape memory behaviors, as shown in Figure 2G, the first-generation EDCs derived from PDMS/10 wt.% ZrO_2 were locally heated to over 1350 °C for 10 min in air in the middle or on one side of the sample with a flame gun. A superalloy mask with a round hole in the middle was used to perform local heat treatment in the middle of the sample.

For the 4D printing and integrated shaping of the ceramic blisk, as shown in Figure 3C,D, a sample of an engine turbine disk (inner and outer diameters of 10 mm and 32 mm, respectively) with 12 blades (24 mm × 9 mm × 0.9 mm) was 3D printed with the ink of PDMS/20 wt.% ZrO_2. The surface of each blade is planar and intersects the ground at 57°. Each blade was then selectively exposed to UV/ozone treatment for 16 h by masking the surface with laser-cut paper. The prepared heterogeneous ceramic precursors were heated to 1000 °C for 2 h, followed by cooling to ambient temperature under vacuum in a resistance heating furnace. The heating and cooling rates were 5 and 10 °C min^{-1}, respectively. Afterward, to realize the shape memory behaviors, as shown in Figure 3F and Figure S15 (Supporting Information), the first-generation EDCs derived from heterogeneous precursors for 4D printed all-ceramic blisk were firstly heated at 1000 °C and then at 1250 °C in air with a tube furnace, resulting in second-generation EDCs.

To demonstrate the mass production capability, 2D AM of the ceramic precursor film (thickness: 0.5 mm) was conducted using blade coating equipment. The precursor film was cured at 100 °C for 30 min and then 150 °C for 20 min. The surface of the precursor film was subjected to UV/ozone treatment for 50 min. Subsequently, the heterogeneous precursor was laser cut into a 10 × 10 array of designed structures within 4.5 min. All processing steps were controlled within 50 min, and with the assistance of a multistation turntable system, as shown in Figure S16 and Movie S11 (Supporting Information), the mass production capability of heterogeneous precursor materials could be as efficient as 30 s per product, on average.

Flame Ablation Testing: Samples with cylindrical woodpile structure of the ceramic precursor material (cylinder diameter, 15 mm; cylinder height, 5.88 mm; nozzle diameter, 0.6 mm; layer thickness, 0.42 mm; center-to-center ligament spacing, 1 mm) were 3D printed using DIW technique. The printed precursors were cured at 150 °C for 30 min in an oven and then heated to 1300 °C for 2 h, followed by cooling to ambient temperature under vacuum in a resistance heating furnace. The porosity of the printed ceramic lattices was 40.8% obtained from the mercury intrusion porosimeter testing. Samples with cylindrical woodpile structure of the IN718 alloy (cylinder diameter, 10.7 mm; cylinder height, 4.2 mm; ligament diameter, 0.3 mm; center-to-center ligament spacing, 0.71 mm) were 3D printed using the selective laser melting technique.

Stoichiometric Al_2O_3 thin films were deposited on 3D printed ceramics using a homemade thermal ALD system. First, the cleaned ceramic specimens were placed in a reaction chamber and evacuated to a base pressure of less than 0.3 Pa. High-purity argon gas was used to purge the reaction chambers. The reaction chamber was heated at a rate of 1°C min^{-1} until the temperature stabilized at 180 °C. To deposit the Al_2O_3 thin films, trimethylaluminum and water precursors were used as reactants, and argon was used as the carrier and purging gas. After the deposition, the reaction chamber was cooled in a vacuum, and the treated specimens were extracted from the chamber by venting after the chamber temperature decreased to less than 50 °C.

Superalloy IN718 samples were used as the substrate material for the TBC process. Commercial NiCrAlY powder (No. 9624, Sulzer-Metco) was used as a bond coating. The agglomerated and sintered ZrO_2–7 wt.% Y_2O_3 (7YSZ) powders used for the top ceramic coating were provided by H.C. Starck (AMPERIT^{TM} 827). Prior to the bond coating, the substrates were degreased and cleaned with gasoline and ethanol, followed by grit blasting with alumina at 0.2 MPa. Subsequently, the samples with bond and ceramic coatings were prepared using an atmospheric plasma spray (APS, MF-P1000, GTV, Germany). The thicknesses of the bond and top ceramic coatings were ≈50 and 80 µm, respectively.

For the flame ablation testing process, the test sample was fixed to the setup with the front surface facing the flame gun. After ignition, a high-temperature gas formed at the nozzle of the gas gun, which was advanced to heat the surface of the sample. The surface temperatures of the samples were monitored in real-time using an infrared thermometer. When the sample temperature reached the target temperature of 1100–1500 °C, the 1 min heat preservation stage was initiated. At this stage, the system dynamically changes the gas flow through an automatic feedback adjustment system to maintain the temperature balance. After the heat preservation stage, the spray gun was withdrawn and the sample surface was cooled using compressed air. To quantify the flame ablation performance of different structural material systems, optical images from the front, back, and side views and weight measurements were obtained and compared before and after the flame ablation tests of each sample. Each data point in Figure 6G represents the average value obtained from two samples as shown in Figures S25–S27 and Table S1 (Supporting Information). The error bars in Figure 6G are estimated as standard deviations from two independent measurements for each data point.

Characterization: Scanning electron microscopy analysis (SEM, Tescan Clara, Tescan; Nova-Nono430, FEI) was used to characterize the structures of the ceramics and UV/ozone films on the surfaces of the ceramic precursors. Transmission electron microscopy (TEM, Titan Themis 200/Strata 400S, FEI) was used to characterize the NCADP structure of the ceramics and the amorphous structure of the SiOC glass. The average composition of the ceramics was measured using energy-dispersive X-ray spectroscopy. To characterize the porous feature inside EDCs, a pore size analyzer (BSD-PS(M), BeiShiDe Instrument) was used to obtain N_2 absorption-desorption isotherms of EDCs. Brunauer–Emmett–Teller analysis and nonlinear density functional theory was used to obtain specific surface area and pore size distribution of EDCs, respectively. A mercury intrusion porosimeter (MicroActive AutoPore V 9600, Micromeritics Instrument) was used to measure the porosity of the printed ceramic lattices. A focused ion beam (FIB; 450S/Talos F200, FEI) was used to prepare the TEM samples. The crystal structures of the ceramics were analyzed through X-ray diffraction (SmartLab, Rigaku). Optical profiler measurements (NPFLEX, Bruker) were obtained for the laser-engraved and mass-produced kirigami samples to determine the 3D morphology. Optical 3D scanning (ATOS Core 200, Abad Deghat Markazi Co.) was performed to quantify the repeatability of the blades of 4D printed all-ceramic blisk. Tension tests (Testpilot-10, Wance) of the precursors were performed using 3D printed solid samples (75 mm × 10 mm × 1 mm), at a displacement rate of 5 mm min^{-1}. Nanoindentation tests (Hysitron TI980, Bruker) were performed on the surface of the UV/ozone film to obtain the modulus for FEA simulation. To analyze the thermal decomposition process

of the precursors, thermogravimetric analysis (TGA, Pyris 1 TGA, Perkin Elmer) and differential scanning calorimetry (DSC, Diamond DSC, Perkin Elmer) tests were performed at a heating rate of 106 °C min^{-1} under a nitrogen flow of 50 mL min^{-1}. Thermal expansion tests (DIL402C, NETZSCH) of the precursors were performed using 3D printed solid samples (20 mm × 20 mm × 4 mm) that were heated to 300 °C at a rate of 5 °C min^{-1}.

Simulation: FEA was performed using commercial software ABAQUS (2016) to examine the deformation behavior during thermal expansion. The UV/ozone film was modeled as an elastic shell. The precursor and UV/ozone film were assumed to be incompressible Neo-Hookean and elastic materials, respectively. The mechanical properties and dimensions of the structures were consistent with experimental measurements. The linear thermal expansion coefficients of PDMS/10 wt.% ZrO_2 and PDMS/20 wt.% ZrO_2, before the transformation to ceramics, were 283 × 10^{-6} and 242 × 10^{-6} $°C^{-1}$, respectively, according to the results of the thermal expansion tests shown in Figure S4D and Figure S13B (Supporting Information). The moduli of PDMS/10 wt.% ZrO_2 and PDMS/20 wt.% ZrO_2 were set as 1.14 and 1.56 MPa, respectively, according to the tension test results shown in Figures S4C and S13A (Supporting Information). During the loading process, a 0–10% strain was applied to obtain the corresponding Young's modulus. The thickness of the UV/ozone film exposed for 8 h was set as 33 µm according to the SEM results shown in Figure S5A, and its modulus was set as 13 MPa according to the nanoindentation results shown in Figure S5B (Supporting Information). The thickness of the UV/ozone film exposed on PDMS/20 wt.% ZrO_2 for 16 h was set as 38 µm according to the SEM results shown in Figure S14A (Supporting Information), and its modulus was set as 20 MPa according to the nanoindentation results shown in Figure S14B (Supporting Information). The modulus of the equivalent film was calculated by assuming that the cross-sections had the same tensile stiffness. Before the significant material transformation, the thermal expansion of the precursors dominated the shape transformation. Thus, only the thermal expansion was considered in the simulations.

Supporting Information

Supporting Information is available from the Wiley Online Library or from the author.

Acknowledgements

This work was supported by the Guangdong Provincial Department of Science and Technology (Key-Area Research and Development Program of Guangdong Province, Grant No. 2020B090923002) (JL); Shenzhen-Hong Kong Science and Technology Innovation Cooperation Zone Shenzhen Park Project (HZQB-KCZYB-2020030) (JL); Research Grants Council of the Hong Kong Special Administrative Region, China (Project No. CityU PDFS2223-1S05) (GL); Major Program of Changsha Science and Technology Project (Project No. kh2003023) (JL); Hong Kong Innovation and Technology Commission via the Hong Kong Branch of National Precious Metals Material Engineering Research Center (JL); Research Grants Council of the Hong Kong Special Administrative Region, China (Project No. AoE/M-402/20) (JL). The authors thank Sida Wang for assisting in the high-resolution movie shooting. The authors thank the helpful discussions with Shimin Zhang, Chengcheng Feng, and Dr. Ying Zhu at CityU-Shenzhen Futian Research Institute. The authors appreciate the assistance of Taorui Wang in the sample preparation at the City University of Hong Kong.

Conflict of Interest

J.L. and G.L. have filed two patents related to this work (U.S. Patent 17500934, 13 October 2021, and U.S. Patent 63509284, 21 June 2023). The organization issuing these two patents is the City University of Hong Kong. J.L., G.L., Z.F.Z., X.F.Z., and X.Y.L. have filed a patent related to this work (U.S. Patent 18182317, 10 March 2023). The organization issuing this patent is the City University of Hong Kong Shenzhen Futian Research Institute. The authors declare that they have no other competing interests.

Data Availability Statement

The data that support the findings of this study are available in the Supporting Information of this article.

Keywords

4D printing, additive–subtractive manufacturing, shape memory ceramics, heterogeneous precursors, polymer-derived ceramics

Received: March 6, 2023
Revised: May 13, 2023
Published online: July 30, 2023

[1] G. Liu, X. Zhang, X. Chen, Y. He, L. Cheng, M. Huo, J. Yin, F. Hao, S. Chen, P. Wang, S. Yi, L. Wan, Z. Mao, Z. Chen, X. Wang, Z. Cao, J. Lu, *Mater. Sci. Eng., R.* **2021**, *145*, 100596.
[2] a) D. A. Walker, J. L. Hedrick, C. A. Mirkin, *Science* **2019**, *366*, 360; b) J. T. Toombs, M. Luitz, C. C. Cook, S. Jenne, C. C. Li, B. E. Rapp, F. Kotz-Helmer, H. K. Taylor, *Science* **2022**, *376*, 308; c) B. E. Kelly, I. Bhattacharya, H. Heidari, M. Shusteff, C. M. Spadaccini, H. K. Taylor, *Science* **2019**, *363*, 1075; d) S. K. Saha, D. Wang, V. H. Nguyen, Y. Chang, J. S. Oakdale, S.-C. Chen, *Science* **2019**, *366*, 105; e) J. R. Tumbleston, D. Shirvanyants, N. Ermoshkin, R. Janusziewicz, A. R. Johnson, D. Kelly, K. Chen, R. Pinschmidt, J. P. Rolland, A. Ermoshkin, E. T. Samulski, J. M. DeSimone, *Science* **2015**, *347*, 1349.
[3] a) P. Kunwar, Z. Xiong, S. T. McLoughlin, P. Soman, *3D Print. Addit. Manuf.* **2020**, *7*, 216; b) P. Kunwar, Z. Xiong, Y. Zhu, H. Li, A. Filip, P. Soman, *Adv. Opt. Mater.* **2019**, *7*, 1900656.
[4] a) D. Zhang, D. Qiu, M. A. Gibson, Y. Zheng, H. L. Fraser, D. H. StJohn, M. A. Easton, *Nature* **2019**, *576*, 91; b) J. H. Martin, B. D. Yahata, J. M. Hundley, J. A. Mayer, T. A. Schaedler, T. M. Pollock, *Nature* **2017**, *549*, 365.
[5] a) Q. Ge, C. K. Dunn, H. J. Qi, M. L. Dunn, *Smart Mater. Struct.* **2014**, *23*, 094007; b) Z. Liu, H. Du, J. Li, L. Lu, Z.-Y. Li, N. X. Fang, *Sci. Adv.* **2018**, *4*, eaat4436.
[6] Q. Zhao, W. Zou, Y. Luo, T. Xie, *Sci. Adv.* **2016**, *2*, e1501297.
[7] Y. Kim, H. Yuk, R. Zhao, S. A. Chester, X. Zhao, *Nature* **2018**, *558*, 274.
[8] H. Cui, D. Yao, R. Hensleigh, H. Lu, A. Calderon, Z. Xu, S. Davaria, Z. Wang, P. Mercier, P. Tarazaga, X. Zheng, *Science* **2022**, *376*, 1287.
[9] F. B. Coulter, A. Ianakiev, *3D Print. Addit. Manuf.* **2015**, *2*, 140.
[10] X. Xia, A. Afshar, H. Yang, C. M. Portela, D. M. Kochmann, C. V. Di Leo, J. R. Greer, *Nature* **2019**, *573*, 205.
[11] a) G. Liu, Y. Zhao, G. Wu, J. Lu, *Sci. Adv.* **2018**, *4*, eaat0641; b) F. L. Bargardi, H. L. e. Ferrand, R. Libanori, A. R. Studart, *Nat. Commun.* **2016**, *7*, 13912; c) D. Zhang, W. Jonhson, T. S. Herng, Y. Q. Ang, L. Yang, S. C. Tan, E. Peng, H. He, J. Ding, *Mater. Horiz.* **2020**, *7*, 1083; d) N. Zheng, J. Hou, H. Zhao, J. Wu, Y. Luo, H. Bai, J. A. Rogers, Q. Zhao, T. Xie, *Adv. Mater.* **2019**, *31*, 1807326; e) K. Huang, H. Elsayed, G. Franchin, P. Colombo, *Addit. Manuf.* **2020**, *33*, 101144; f) C. Wang, W. Ping, Q. Bai, H. Cui, R. Hensleigh, R. Wang, A. H. Brozena, Z. Xu, J. Dai, Y. Pei, C. Zheng, G. Pastel, J. Gao, X. Wang, H. Wang, J.-C. Zhao, B. Yang, X. Zheng, J. Luo, Y. Mo, B. Dunn, L. Hu, *Science* **2020**, *368*,

521; g) Z. C. Eckel, C. Zhou, J. H. Martin, A. J. Jacobsen, W. B. Carter, T. A. Schaedler, *Science* **2016**, *351*, 58.
[12] a) Y. Xu, Y. Li, N. Zheng, Q. Zhao, T. Xie, *Nat. Commun.* **2021**, *12*, 4261; b) F. Kotz, K. Arnold, W. Bauer, D. Schild, N. Keller, K. Sachsenheimer, T. M. Nargang, C. Richter, D. Helmer, B. E. Rapp, *Nature* **2017**, *544*, 337.
[13] C. Vakifahmetoglu, D. Zeydanli, P. Colombo, *Mater. Sci. Eng., R.* **2016**, *106*, 1.
[14] P. Warnke, K. Cuhls, U. Schmoch, L. Daniel, L. Andreescu, B. Dragomir, R. Gheorghiu, C. Baboschi, A. Curaj, M. Parkkinen, 100 Radical Innovation Breakthroughs for the Future, **2019**.
[15] D. Kim, I. Ferretto, C. Leinenbach, W. Lee, *Adv. Mater. Interfaces* **2022**, *9*, 2200171.
[16] a) M. V. Swain, *Nature* **1986**, *322*, 234; b) A. Lai, Z. Du, L. Gan Chee, A. Schuh Christopher, *Science* **2013**, *341*, 1505; c) K. T. Faber, *Science* **2013**, *341*, 1464; d) H. Gu, J. Rohmer, J. Jetter, A. Lotnyk, L. Kienle, E. Quandt, R. D. James, *Nature* **2021**, *599*, 416; e) E. L. Pang, G. B. Olson, C. A. Schuh, *Nature* **2022**, *610*, 491.
[17] a) J. Cawley, P. Wei, Z. Liu, W. Newman, B. Mathewson, A. Heuer, presented at Int. Solid Freeform Fabrication Symp, Austin, August 7–9, **1995**; b) G. Hagen, T. Kopp, S. Ziesche, U. Partsch, E. Ruprecht, Additional Papers and Presentations **2012**, *2012*, 000341.
[18] Y. Tao, Y.-C. Lee, H. Liu, X. Zhang, J. Cui, C. Mondoa, M. Babaei, J. Santillan, G. Wang, D. Luo, *Sci. Adv.* **2021**, *7*, eabf4098.
[19] F. Momeni, J. Ni, *Engineering* **2020**, *6*, 1035.
[20] a) N. P. Padture, *Nat. Mater.* **2016**, *15*, 804; b) J. H. Perepezko, *Science* **2009**, *326*, 1068.
[21] R. Wang, P. Zhu, W. Yang, S. Gao, B. Li, Q. Li, *Mater. Des.* **2018**, *144*, 304.
[22] S.-J. Yang, W.-J. Song, D. B. Dingwell, J. He, H.-B. Guo, *Rare Met.* **2022**, *41*, 469.
[23] X. Zhang, Z. Deng, H. Li, J. Mao, C. Deng, C. Deng, S. Niu, W. Chen, J. Song, J. Fan, M. Liu, K. Zhou, *Npj Mater. Degrad.* **2020**, *4*, 31.
[24] N. P. Padture, M. Gell, E. H. Jordan, *Science* **2002**, *296*, 280.
[25] D. R. Clarke, M. Oechsner, N. P. Padture, *MRS Bull.* **2012**, *37*, 891.
[26] L. Li, C. Jia, Y. Liu, B. Fang, W. Zhu, X. Li, L. A. Schaefer, Z. Li, F. Zhang, X. Feng, N. Hussain, X. Xi, D. Wang, Y. H. Lin, X. Wei, H. Wu, *Mater. Today* **2022**, *54*, 72.
[27] National Academies of Sciences, Engineering, and Medicine, *Advanced Technologies for Gas Turbines*, National Academies Press, Washington, DC **2020**.
[28] J. Zhu, H. Zhou, C. Wang, L. Zhou, S. Yuan, W. Zhang, *Chin. J. Aeronaut.* **2021**, *34*, 91.
[29] G. Liu, Y. He, P. Liu, Z. Chen, X. Chen, L. Wan, Y. Li, J. Lu, *Engineering* **2020**, *6*, 1232.
[30] N. Bowden, S. Brittain, A. G. Evans, J. W. Hutchinson, G. M. Whitesides, *Nature* **1998**, *393*, 146.
[31] M. A. Skylar-Scott, J. Mueller, C. W. Visser, J. A. Lewis, *Nature* **2019**, *575*, 330.